Energy Material Advances
A SCIENCE PARTNER JOURNAL

RESEARCH ARTICLE

Conductive Framework-Stabilized Zn-Metal Anodes for High-Performance Zn-Ion Batteries and Capacitors

Zhe Gong[1], Zhuo Li[1], Pengfei Wang[1,2], Kai Jiang[3], Zhaowen Bai[3], Kai Zhu[1,3*], Jun Yan[1], Ke Ye[1], Guiling Wang[1], Dianxue Cao[1*], and Guohua Chen[3,4*]

[1]Key Laboratory of Superlight Materials and Surface Technology of Ministry of Education, College of Materials Science and Chemical Engineering, Harbin Engineering University, Harbin 150001, P.R. China. [2]Key Laboratory of Polymer and Catalyst Synthesis Technology of Liaoning Province, School of Environmental and Chemical Engineering, Shenyang University of Technology, Shenyang 110870, P.R. China. [3]Department of Mechanical Engineering, The Hong Kong Polytechnic University,Hung Hom, Kowloon, Hong Kong SAR, P.R. China. [4]School of Energy and Environment, City University of Hong Kong, Hong Kong 999077, P.R. China.

*Address correspondence to: kzhu@hrbeu.edu.cn (K.Z.); caodianxue@hrbeu.edu.cn (D.C.); guohchen@cityu.edu (G.C.)

Citation: Gong Z, Li Z, Wang P, Jiang K, Bai Z, Zhu K, Yan J, Ye K, Wang G, Cao D, et al., Conductive Framework-Stabilized Zn-Metal Anodes for High-Performance Zn-Ion Batteries and Capacitors. *Energy Mater. Adv.* 2023;4:Article 0035. https://doi.org/10.34133/energymatadv.0035

Submitted 11 December 2022
Accepted 3 May 2023
Published 14 June 2023

Aqueous zinc (Zn)-based energy storage devices possess promising applications for large-scale energy storage systems due to the advantage of high safety, low price, and environment-friendliness. However, their development is restricted by dendrite growth and hydrogen evolution issues from the Zn-metal anode. Herein, a facile stress-pressing method is reported for constructing a grid zinc anode (GZn) with a conductive framework. The highly conductive copper (Cu)-mesh framework reduces electrode hydrogen evolution and increases electrode conductivity. Meanwhile, the in situ-formed Cu-Zn nano-alloy stabilizes the Zn deposition interface. As a result, the GZn symmetrical cell presents a low overpotential of 49 mV after cycling for 1,200 h (0.2 $\mathrm{mA{\bullet}cm^{-2}}$). In addition, GZn displays its potential application as a universal anode for Zn-ion capacitors and batteries. An activated carbon||GZn Zn-ion capacitor delivers a stable cycling performance after 10,000 cycles at 5 $\mathrm{A{\bullet}g^{-1}}$ and MnO_2||GZn Zn-ion batteries exhibit satisfactory cycle stability and excellent rate performance. This demonstrates that GZn appears to be a promising universal anode for Zn-ion capacitors and batteries.

Introduction

Rechargeable aqueous metal-ion batteries (Mg^{2+}, Zn^{2+}, Fe^{2+}, and Al^{3+}) present unique advantages, such as their high natural abundance, high electrolyte safety, and environment-friendliness [1]. Among them, zinc (Zn) metal can be directly employed as an electrode with the unique advantage of low redox potential (−0.76 V vs. standard hydrogen electrode), high theoretical specific capacity (820 $\mathrm{mAh{\bullet}g^{-1}}$), and large earth abundance. Thus, Zn-ion batteries have become one of the most attractive aqueous batteries [2–6]. In recent years, several kinds of cathode materials have been employed in Zn-ion batteries, such as vanadium-based oxides, manganese oxides, and metal ferricyanide, and great strides have been made, which has strongly supported the production of Zn-ion batteries with high energy density [7,8]. Meanwhile, capacitor-type materials, such as active carbon (AC), have become cathode choices for aqueous Zn-based devices, called Zn-ion capacitors, to meet the requirement of high power density. However, for either Zn-ion batteries or capacitors, an ignored limiting factor has been the stability of Zn-metal anodes during resting and cycling. The excessive local current on the Zn electrode surface promotes uneven Zn-ion deposition, thus aggravating Zn protrusion growth and dendrite formation [9–12]. Undesired Zn dendrites can peel off from the Zn surface and become dead Zn, reducing the Zn utilization rate and cycling ability [13,14]. Meanwhile, Zn dendrite formation leads to enhancement of hydrogen evolution on the electrode/electrolyte interface, resulting in the electrolyte consumption and poor cycling performance [15–18]. Thus, it is highly required to design and fabricate a Zn anode without dendrite persecution.

Recently, many effective strategies have been developed to suppress the Zn dendrite growth, including as surface modifications [19–23], structural designs [24–28], and electrolytes [29–33]. Among these strategies, surface modifications and structural designs are capable and promising approaches for improving Zn anode's properties. Zn-anode surface modification could regulate electrode/electrolyte interfaces and guide uniform Zn deposition [34,35]. Cao et al. [36] have introduced a Zn-phosphorus solid-solution alloy as a protective layer, using an electrodeposition method, to facilitate ion transfer and reduce the electrochemical activation energy during Zn stripping/plating processes. Cai et al. [37] have prepared a Cu/Zn composite via an immersion and calcination 2-step method. During the electrochemical process, the Cu-Zn nano-alloy was formed in situ on the surface, which leads to good anticorrosion behavior and stable cycling performance. Constructing a Zn electrode with the conductive host is another promising means for improving the intrinsic capability of metal anodes. The employment of a conductive current collector, especially with a 3-dimensional structure, could increase the electrode surface area and reduce local current density, leading to uniform deposition of Zn ions. For example, Li's team [38] has synthesized tin (Sn)-coated carbon cloth as a conductive substrate for Zn-ion deposition, thus affording a low deposition overpotential of 90 mV and inhibiting hydrogen evolution. An et al. [39] have constructed a nitrogen/oxygen (N/O) double-doped carbon array on a Cu foam surface to effectively improve the reversibility of Zn plating/stripping, leading to a 240-h cycling ability. This structure was conducive for guiding uniform Zn-ion deposition and achieved an average Coulombic efficiency of 98.2% at a current density of 1 mA•cm^{-2} for 350 cycles. However, for these Zn electrodes, their complicated fabrication processes might not be suitable for large-scale production. It has remained a challenge to construct a capable dendrite-free Zn anode through a convenient process.

In this study, a grid Zn-metal anode (GZn) was designed and constructed via stress-pressing a commercial Cu mesh onto Zn foil. The highly conductive Cu-mesh framework ensured gridded Zn plating/striping. Meanwhile, a Cu-Zn nanoalloy layer was formed in situ during cycling, which thus provided a stable deposition interface. As a result, the symmetric GZn cell presented a smaller overpotential than that of symmetric bare Zn (BZn). In addition, Zn-ion hybrid capacitors were assembled by coupling AC cathodes and GZn anodes, which displayed outstanding cycle stability, benefiting from dendrite-free GZn anodes. Furthermore, GZn||MnO_2 full cells also presented stable cycling performance and laudable rate performance. This study demonstrated the potential application of GZn as a universal anode for Zn-based aqueous capacitor and batteries.

Materials and Methods

Fabrication of grid Zn-metal anode (GZn)

The Zn foil (purity 99.99%, Zhengying Co., Ltd., China) was sonicated in ethanol (Tianli Chemical Reagent Co., Ltd., Tianjin, China) for 5 min to remove surface impurities. Subsequently, the clean Zn foil was placed in a 0.5 M hydrochloric acid (Xintian Fine Chemical Factory, China) solution for 30 s to remove impurities. After washing with deionized water, bare Zn (BZn) was obtained. Then, the Cu mesh (Yingtan Zhongzhen Co., Ltd., China) was pressed onto the BZn surface under a pressure of 15 MPa to yield GZn.

Preparation of MnO_2

The β-manganese dioxide (β-MnO_2) was prepared by a hydrothermal method. First, 1.52 g of manganese sulfate ($MnSO_4$) and 0.1 g of sodium sulfate (Na_2SO_4, Sinopharm Chemical Reagent Co., Ltd., Shanghai, China) were added to 15 ml of deionized water and stirred until fully dissolved. Another 0.24 g of potassium permanganate ($KMnO_4$, Aladdin Reagent Co., Ltd., Shanghai, China) was added to 15 ml of deionized water and stirred until dissolved. Subsequently, the $KMnO_4$ solution was added to the Na_2SO_4/$MnSO_4$ solution under constant stirring. The resulting solution was stirred at room temperature for 30 min and then transferred to a 50-ml reaction kettle. The hydrothermal reaction was conducted at 160°C for 12 h, after which the reacted solution was cooled and centrifuged and the resulting pellet was washed several times with deionized water and alcohol. The solid was finally dried in an oven at 80°C for 24 h to obtain rod-shaped β-MnO_2.

Material characterization

A scanning electron microscope (SEM, JSM-6480, JEOL Ltd., Tokyo, Japan) and transmission electron microscope (TEM, Tecnia G2-STWIN, FEI Co., Hillsboro, OR, USA) were employed to observe electrode surface morphologies. Energy-dispersive spectrometry (EDS, Tecnia G2-STWIN, FEI Co) was used to analyze the surface element distribution. An x-ray diffractometer (D/max-TTR III, Rigaku Corp., Tokyo, Japan) was utilized to analyze electrode crystal structure at a scan rate of 10°•min^{-1}, an accelerating current of 150 mA, and an accelerating voltage of 40 kV.

Electrochemical measurements

Symmetric cells were assembled with Zn electrodes, which were BZn or GZn and the electrolyte 2 M $ZnSO_4$ (Macklin Co., Ltd., China). For the full cell, the cathode was fabricated by mixing MnO_2, a conductive agent (commercial graphene, Huasheng Graphite Co., Ltd., China), and a binder, polyvinylidene fluoride (PVDF, Kejing Co., Ltd., China), in a mass ratio of 7/2/1. The slurry was coated on carbon cloth and the electrode was dried under 80°C in a vacuum oven for 12 h. Mass loading of active materials in the electrode was 1.5 to 2.0 mg•cm^{-2}. The BZn or GZn anode, MnO_2 cathode, glass fiber separator, and the electrolyte (2 M $ZnSO_4$ and 0.1 M $MnSO_4$) were assembled into BZn||MnO_2 or GZn||MnO_2 full cells. The cells were charged and discharged with a capacity of 0.2 mA•h•cm^{-2}.

For the cathode of the Zn-ion hybrid capacitor, AC (purity 99.5%, XFNANO Inc., Nanjing City, China), a conductive agent (acetylene black, Kejing Co., Ltd., China), and a binder (PVDF) were mixed in a mass ratio of 7/2/1. The subsequent process was the same as that for the MnO_2 electrode. The BZn or GZn anode, AC cathode, glass fiber separator, and electrolyte (2 M $ZnSO_4$) were assembled into BZn||AC or GZn||AC hybrid capacitors.

Galvanostatic cycling and rate performance were performed on a Neware test system (CT-4008T, Neware Technology, Ltd., Shenzhen, China). Cyclic voltammetry (CV) and electrochemical impedance spectroscopy (EIS) curves were acquired using an EC-lab (VMP3, BioLogic Science Instruments, Seyssinet-Pariset, France). EIS was carried out with a frequency range from 10 mHz to 100 kHz. A 3-electrode system was assembled for linear sweep voltammetry (LSV), with BZn or GZn used as the working electrode, an Ag/AgCl electrode as the reference electrode, graphite as the counter electrode, and 2 M $ZnSO_4$ as the electrolyte. LSV was assessed using an Autolab PGSTAT (Metrohm Autolab B. V., Utrecht, The Netherlands) at a scan rate of 5 mV•s^{-1}.

Results

The preparation process for grid Zn (GZn) electrodes is shown in Fig. 1A. Commercial Cu mesh was pressed onto cleansed commercial BZn under 15 MPa. SEM images of the product

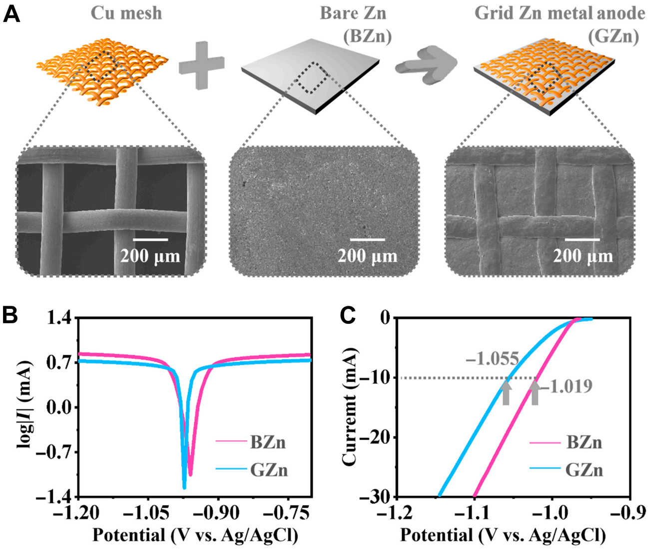

Fig. 1. Schematic diagram and SEM images of GZn electrode preparation (A). Corrosion curves of BZn and GZn (B). LSV curves of BZn and GZn (C).

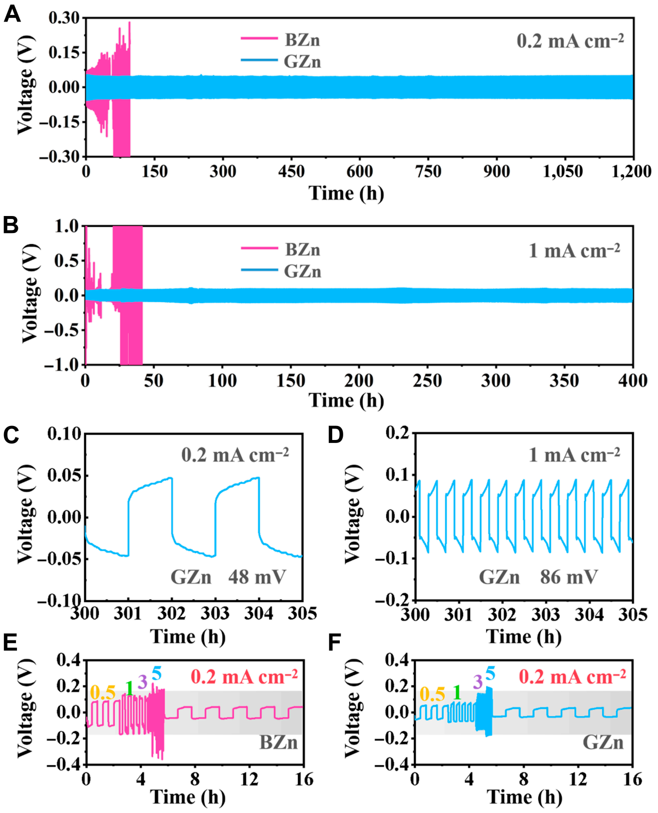

Fig. 2. Voltage–time curves of BZn and GZn at 0.2 (A) and 1 mA cm^{-2} (B, 0.2 mA•h•cm^{-2}). Details of voltage–time curves of GZn at 0.2 (C) and 1 mA•cm^{-2} (D, 0.2 mA•h•cm^{-2}). Rate performances of BZn (E) and GZn (F) at current densities from 0.2 to 5 mA•cm^{-2} (0.2 mA•h•cm^{-2}).

demonstrated the smooth surface of the copper mesh and Zn foil in their initial states. The Cu mesh consisted of crossed Cu wires of ~140 μm diameter. Under pressure, the Cu mesh was implanted into the Zn foil and marked off a ~300 × 300 μm grid, enhancing the composite electrode's electrical conductivity and surface area.

The corrosion and hydrogen evolution behavior of GZn and BZn in the typical 2 M $ZnSO_4$ electrolyte were investigated by evaluating the corrosion curves of electrode corrosion resistance (Fig. 1B). Tafel extrapolation was employed to derive the corrosion current densities. With decreasing corrosion current density, the corrosion resistance of the material increased and the corrosion process slowed down. GZn electrodes showed a lower corrosion current density (4.083 mA•cm^{-2}) than that of BZn (5.102 mA•cm^{-2}). This result suggested that GZn possessed better corrosion resistance than BZn and that the introduction of a Cu skeleton reduced the influence of corrosion during cycling. Soaking experiments were carried out to better observe the morphology changes of electrode surface. The soaking solution was 2 M $ZnSO_4$ electrolyte. The morphology of electrodes soaked for 1, 10, and 50 h were characterized by SEM (Fig. S1). For BZn, with the increase of soaking time, the surface flaky by-products gradually increased. In contrast, only a few particles attached to the surface of GZn after soaking. The difference in surface morphology proved that the corrosion resistance of GZn to electrolyte was enhanced. LSV was carried out to verify the hydrogen evolution performance of the electrode (Fig. 1C). GZn required a potential of −1.019 V to reach 10 mA, which was lower than that of BZn (−1.055 V), suggesting reduced hydrogen evolution on GZn. Hydrogen evolution leads to local pH changes due to OH^- concentration accumulation and promotes the generation of $Zn(OH)_2$ by-products. In addition, undesired hydrogen can also cause a battery to swell or even explode. Therefore, the anticorrosion and inactive hydrogen evolution ability observed here were beneficial for improving the electrochemical performance of GZn.

The effects of the Cu mesh in protecting the Zn anode were explored by constructing symmetric cells, with GZn or BZn and 2 M $ZnSO_4$ electrolyte, to examine their electrochemical performance (Fig. 2). GZn||GZn symmetric cells displayed smaller voltage fluctuations and a longer lifetime than BZn||BZn symmetric cells. At a current density of 0.2 mA•cm^{-2}, GZn||GZn cells demonstrated stable voltage profiles for 1,200 h with a low voltage hysteresis of 49 mV (Fig. 2A), suggesting a highly reversible Zn plating/stripping process with the assistance of the Cu grid. Meanwhile, GZn presented 400 h and 225 h of cycling at a current density of 1 and 3 mA•cm^{-2}, respectively, than BZn (Fig. 2B and Fig. S2). In contrast, BZn||BZn cells showed gradually increased overpotential at each current density, which might have been caused by dendrite generation. The enlarged views of the GZn voltage curves after 300 h of operation are shown in Fig. 2C and D. GZn showed a regular charge–discharge curve in each cycle, accompanied by Zn's stable plating/stripping process. In addition, GZn was tested for cycle performance at extremely high current density (1 to 100 mA•cm^{-2}) and capacity (1 to 50 mAh•cm^{-2}), showing strong competitiveness (Figs. S3 and S4). The cycle performance of different Zn metal anodes is shown in Table S1 [40–45]. The results indicated that the GZn electrode had potential electrochemical performance. The rate performances of GZn and BZn anodes are obtained at various current densities from 0.2 to 5 mA•cm^{-2} (Fig. 2E). GZn electrodes displayed a lower overpotential without clear fluctuations than did BZn, indicating the stable and dendrite-free surface of GZn during the Zn-ion plating/stripping process (Fig. 2F).

Ex situ SEM measurements were performed to better understand the plating/stripping behavior of BZn and GZn. BZn presented a smooth surface but with some inconspicuous defects (Fig. 3A and D). After 10 cycles, BZn showed an irregular surface with dendritic Zn and hollows (Fig. 3B and E). With cycling (100 cycles), the Zn surface became chaotic and many pits were observed. Meanwhile, dendritic Zn became larger and hung with many glass fibers, which might have peeled from the separator (Fig. 3C and F). The close contact observed between the Cu mesh and Zn foil ensured the transfer of electrons in GZn (Fig. 3G and J). No Zn dendrites appeared on the Cu mesh and underlying Zn foil after 10 cycles (Fig. 3H and K). After 100 cycles, there was still no obvious dendrites on the GZn electrode (Fig. 3I and J). The surface of the Cu mesh was covered by deposited Zn, and the presence of small pits on the underlying Zn surface was attributed to Zn stripping. The SEM image of the cross section of the GZn electrode after cycling showed that the Cu mesh was embedded on the Zn metal surface without dendrite production (Fig. S5A). The corresponding EDS mapping confirmed the presence of deposited Zn on the Cu mesh surface (Fig. S5C and D). In contrast, cross-section deposition of the cycled BZn electrode was not compacted (Fig. S5B), which was not conducive to stable electrochemical performance. This demonstrated that GZn presented a more stable surface without dendritic Zn growth, leading to capable cycling stability.

In order to better research the principle of electrode surface during Zn deposition/stripping, BZn and GZn with different

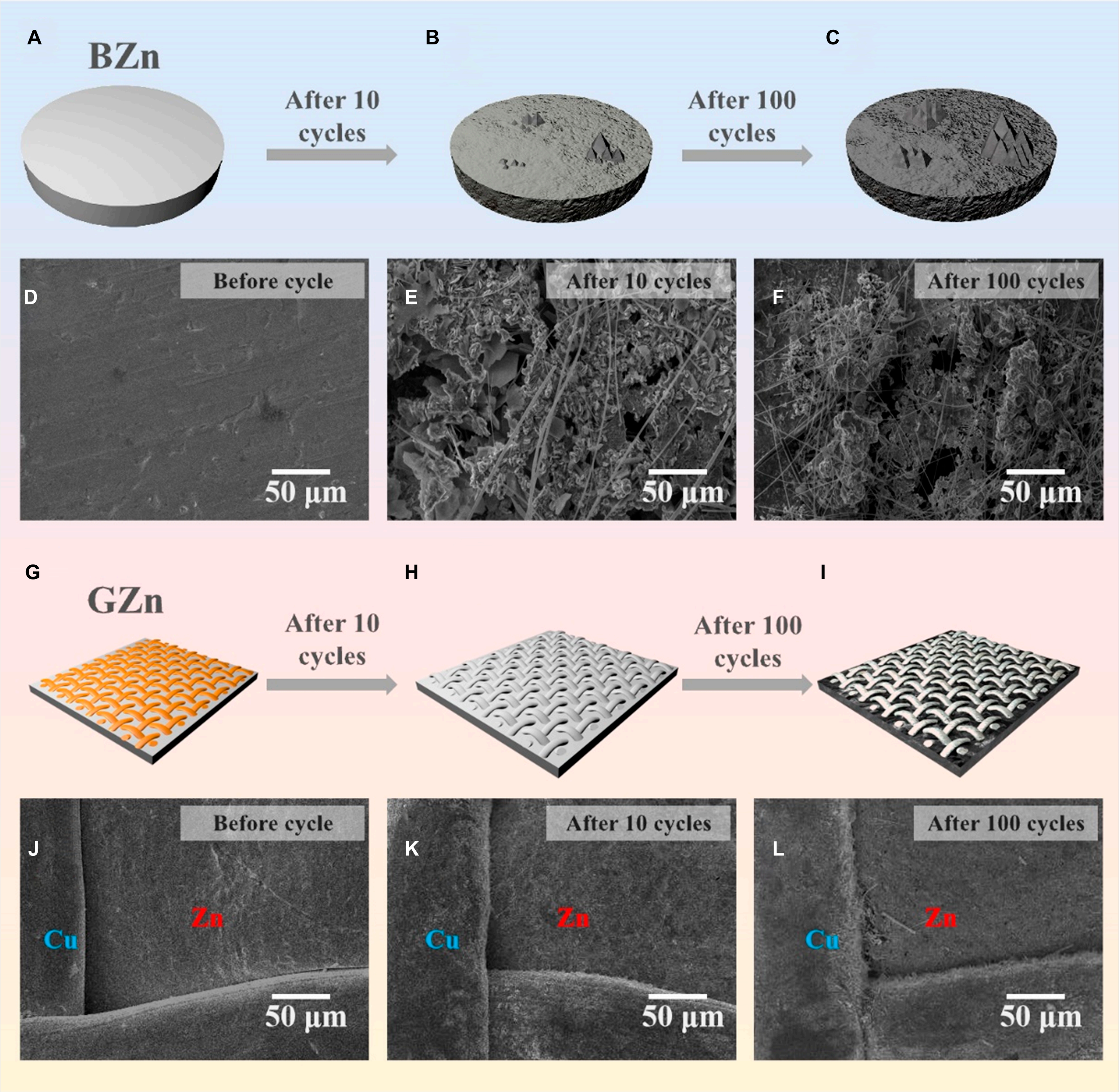

Fig. 3. Topographic schematic diagrams of BZn and GZn before cycling (A and G) and after 10 (B and H) and 100 (C and I) cycles at 1 mA•cm^{-2}. SEM images of BZn and GZn before cycling (D and J) and after 10 (E and K) and 100 (F and L) cycles at 1 mA•cm^{-2}.

deposition/stripping capacities were tested by SEM. When Zn was plated on GZn, with the increase of deposition capacity, the Zn attached to Cu wires increased (Fig. S6A to D). After peeling off a large amount of plated Zn, the surface morphology of the electrode had no obvious change (Fig. S7A to D). In contrast, when Zn was deposited on BZn in a large capacity, it would converge into block structures (Fig. S6E to H). With the stripping of Zn, the loss of Zn was large, resulting in a huge depression (Fig. S7E to H) on the electrode surface. In addition, the morphology of GZn after a long cycle was characterized, which showed a uniform morphology, and Zn was distributed on the surface of the Cu mesh (Fig. S8). Therefore, it was speculated that with the development of the cycle, Zn was gradually deposited on the Cu mesh with better conductivity and more concentrated current, and it showed a stable dendrite-free structure during repeated plating/stripping (Fig. S9).

X-ray diffractometry (XRD) was employed to explore crystal face changes of the electrode and the relationship between the crystal structure and cell performance. After 1, 10, and 100 cycles at 1 mA•cm^{-2}, the symmetrical cells with BZn or GZn were disassembled to measure their XRD (Fig. 4A and B). Both BZn and GZn displayed typical XRD patterns belonging to Zn, with a hexagonal close-packed structure. The 5 peaks at about 36.2, 39.1, 43.1, 70.1, and 70.7, were ascribed to the (002), (100), (101), (103), and (110) planes of Zn, respectively [46]. The peaks of Zn in BZn and GZn were almost the same after one cycle and the Cu crystal diffraction peak observed in the XRD pattern of GZn. After 100 cycles, the XRD of BZn showed a new diffraction peak belonging to zinc hydroxide ($Zn(OH)_2$), which came from the by-product on the BZn surface [47]. Hydrogen evolution on the electrode surface resulted in a large amount of H+ consumption and increased local OH^- concentration. Therefore, Zn ions were easily recruited into $Zn(OH)_2$ precipitation at the position with high OH^- concentration, thus leading to the consumption of electrolyte and dead Zn. In contrast, there was no clear peak belonging to such by-product in GZn (Fig. 4B). This demonstrated that there was less by-product generation on the GZn surface due to the suppressed hydrogen evolution reaction (HER). Zn deposition on the Cu mesh surface was collected and measured by EDS testing (Fig. 4C). EDS images showed the uniform distribution of Cu and Zn in the particles, suggesting a Zn_xCu_y mixture or alloy. High-resolution TEM (HR-TEM) images showed clear lattice fringes of 0.240, 0.105, and 0.258 nm belonging to the (321), (220), and (222) planes of Cu-Zn alloys [37], respectively (Fig. 4D). These results demonstrated Cu-Zn nano-alloy generation during the repeated plating/stripping process of Zn. In addition, the TEM image of Zn metal surface indicated that Cu-Zn alloy was only produced on the Cu mesh (Fig. S10).

The deposition behavior of Zn ions on BZn and GZn surfaces was analyzed by chronoamperometry (Fig. S11). In a chronoamperometry curve, the diffusion process is related to the time it takes for the current to reach steady state. During a 150-s test, the current density of BZn continued to increase, indicating that its surface was always a 2-dimensional (2D) diffusion process. During the 2D diffusion process, Zn ions tended to accumulate at the electrode tip, which promoted Zn dendrite generation and growth [48,49]. In contrast, the current density of GZn tended to stabilize after 33 s, which indicated that, after a brief 2D diffusion process, the GZn surface transformed into

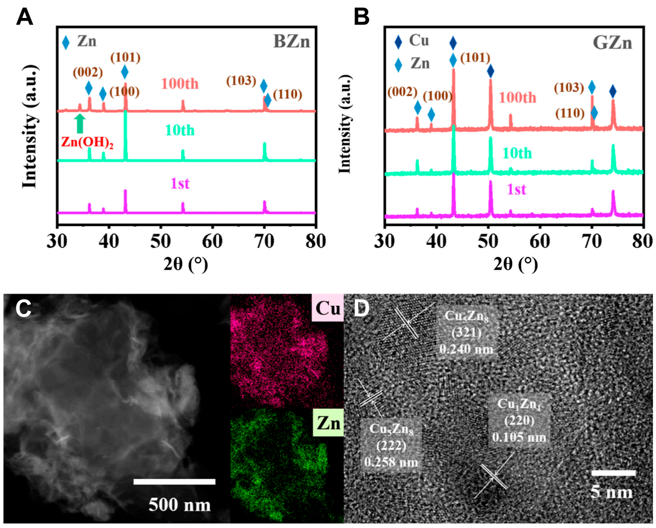

Fig. 4. XRD patterns of BZn (A) and GZn (B) after different cycle numbers. Energy-dispersive spectrometry (C) and HR-TEM images (D) of GZn after cycling.

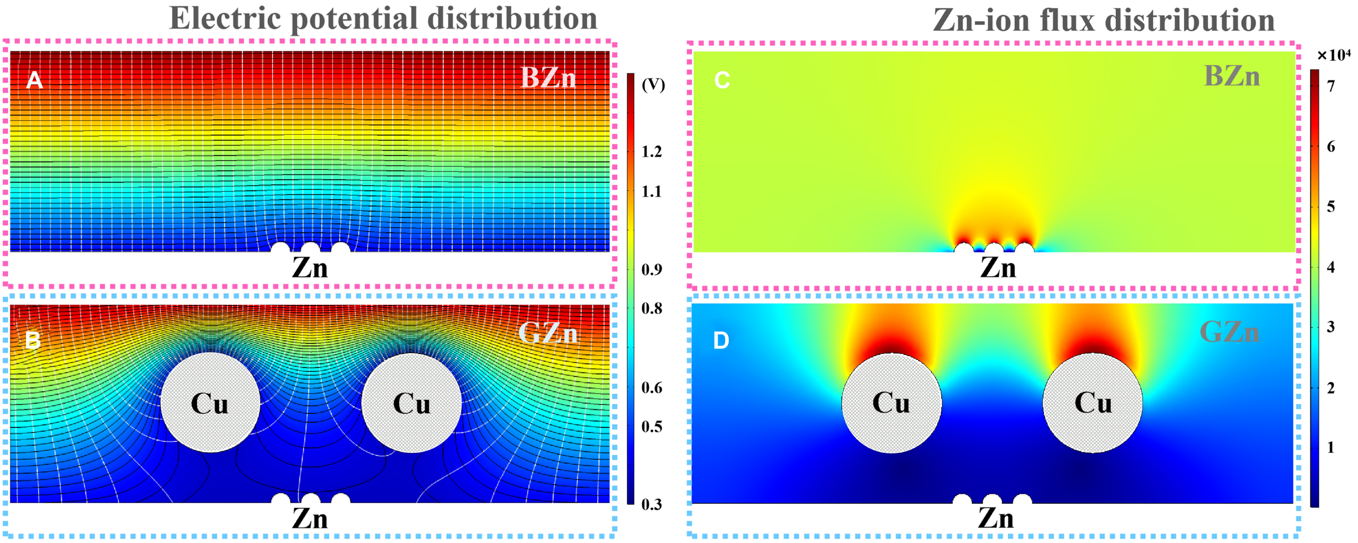

Fig. 5. COMSOL simulations of the electric potential distribution and Zn-ion flux distribution on BZn (A and C) and GZn (B and D).

a 3-dimensional (3D) diffusion process that tended to be deposited horizontally. Also, the 3D diffusion process was always maintained in subsequent depositions. The above results indicated that the addition of a Cu mesh improved Zn-ion diffusion on the electrode surface, which was beneficial for the formation of dendrite-free surface morphology.

COMSOL simulations were used to better understand the Zn deposition process on GZn surfaces. COMSOL simulations of the surface potential distributions for BZn and GZn revealed small convex defects on the BZn surface and the BZn potential at ~453 mV (Fig. 5A). After adding the Cu grid, the potential around GZn dropped to ~377 mV due to modulation of the potential distribution by the conductive active area provided by Cu fibers (Fig. 5B). The reduction of the potential slowed down the HER, such that GZn was less prone to hydrogen evolution than BZn, which was consistent with previous hydrogen evolution test results. COMSOL simulations of Zn-ion flux on BZn and GZn surface showed that the small bumps on the BZn surface led to local Zn-ion accumulation (Fig. 5C), such that Zn dendrites continued to grow at the bumps. The addition of a Cu grid on the GZn surface effectively avoided this "tip effect" and reduced the Zn-ion flux on the underlying Zn foil, enabling it to achieve a dendrite-free morphology after cycling (Fig. 5D). Therefore, GZn was a beneficial strategy for improving cycling stability.

The utility of the application of GZn electrodes was verified by assembling a GZn||AC hybrid capacitors with AC cathodes and GZn anodes (Fig. 6A). For Zn-ion hybrid capacitors, the anode side was accompanied by Zn-ion plating and stripping during the charge and discharge process. The cathode side was dominated by anion desorption and adsorption in the AC. Compared with the CV curves of BZn||AC (Fig. S12), the CV curves of GZn||AC (Fig. 6B) were closer to a typical rectangle, suggesting better capacitive behavior. The BZn||AC hybrid capacitor displayed a gradually decreased capacity during cycling and its capacity retention rate was only 59% after 8,000 cycles (Fig. 6C). In contrast, the GZn||AC hybrid capacitor had a capacity of 61.8 mA•h•g^{-1} after 8,000 cycles at 5 A•g^{-1}, with the capacity retention rate at ~100%.

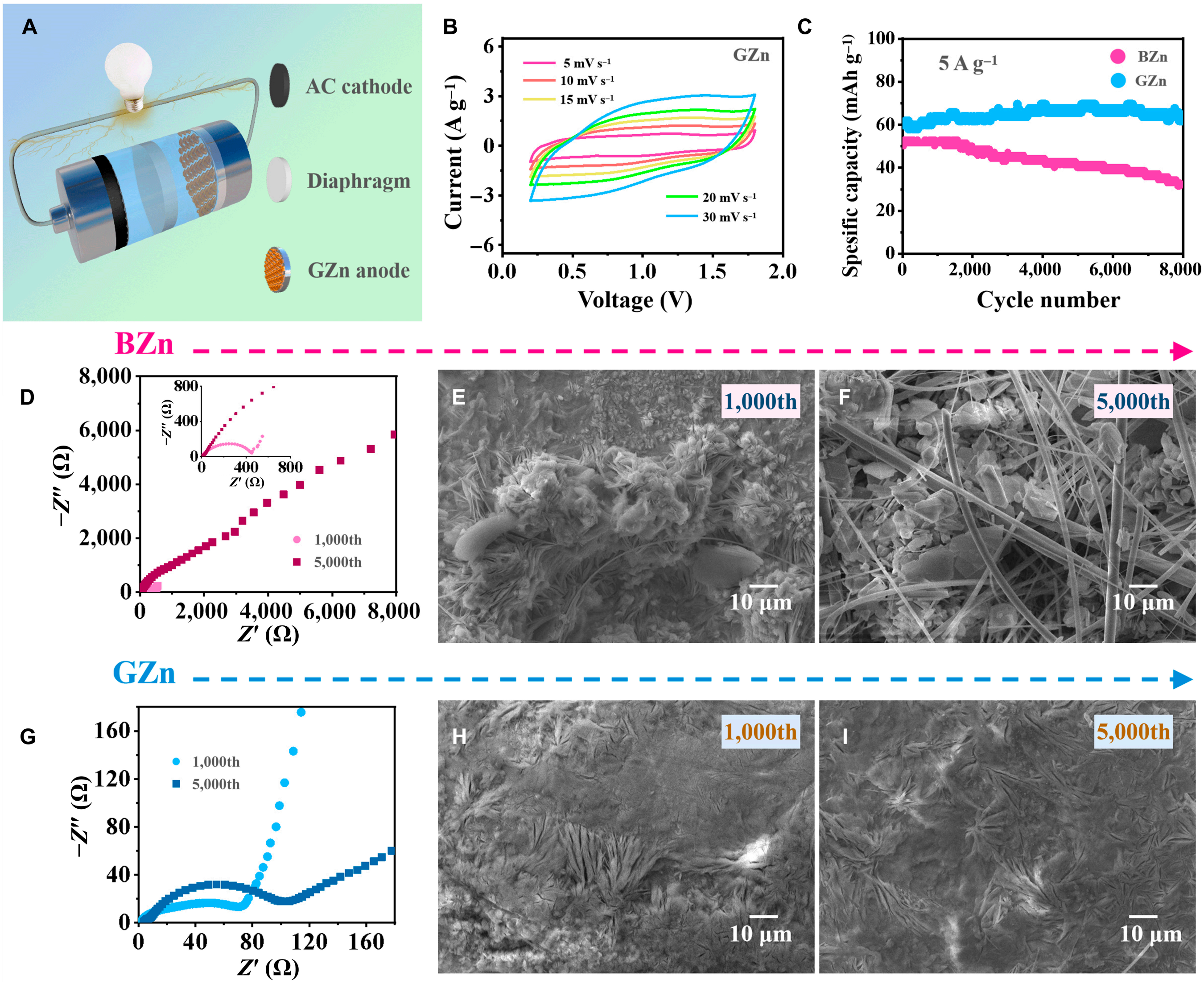

Fig. 6. Schematic diagram of GZn||AC hybrid capacitor assembly (A). CV curves of GZn||AC hybrid capacitor at different scan rates (B). Cycle performance of BZn||AC and GZn||AC hybrid capacitors (C). Nyquist plots of BZn||AC (D) and GZn||AC (G) hybrid capacitors. SEM images of BZn (E and F) and GZn (H and I) after the 1,000th and 5,000th cycle, respectively, at 5 A•g^{-1}.

Observation of Nyquist plots of the BZn||AC hybrid capacitor in different cycles showed that the impedance was 412 Ω after 1,000 cycles, which increased to 2,560 Ω after 5,000 cycles (Fig. 6D and Figs. S13A and S14). This increased impedance was related to by-product generation on the BZn surface. After 1,000 cycles, large and uneven massive Zn on the BZn surface was observed in SEM images (Fig. 6E). After 5,000 cycles, the accumulation of by-products on the BZn surface became worse and a large amount of Zn dendrite tangles, with glass fibers from the separator, were observed (Fig. 6F). The GZn||AC hybrid capacitor showed no great change in charge transfer resistance, from 61 to 83 Ω, after 5,000 cycles, which was attributed to high Cu conductivity and the absence of by-product and dendritic Zn (Fig. 6G). SEM image results indicated that there was no block Zn dendrite formation after cycling (Fig. 6H and I). The flat electrode surface demonstrated the uniform deposition interface, which was conducive to charge transport.

Comparison of the rate performance of BZn||AC and GZn||AC hybrid capacitors at current densities of 0.5, 1, 2, 5, and 10 A•g^{-1} clearly showed that the GZn||AC hybrid capacitor exhibited a greater capacity than the BZn||AC hybrid capacitor at each current density (Fig. S15a). The voltage profiles of the rate performance more intuitively showed the charge–discharge process of these hybrid capacitors (Fig. S15B and C). The BZn||AC hybrid capacitor underwent more severe polarization with increased test current density and its voltage drop was 0.3 V at 10 A•g^{-1}, resulting in a capacity of 44.2 mA•h•g^{-1}. Meanwhile, the GZn||AC hybrid capacitor retained a high capacity of 54.2 mA•h•g^{-1} at 10 A•g^{-1}, which was related to its lower voltage drop of 0.2 V.

Full cells with a MnO_2 cathode and Zn anode were assembled to demonstrate the application of the GZn electrode for Zn-ion batteries. The XRD pattern of the prepared MnO_2 corresponded well with the standard card for pyrolusite (β-MnO_2, PDF#024-0735; Fig. S16). SEM imaging showed that MnO_2 was a regular rod-like structure with a diameter of ~0.3 μm (Fig. S17). Examination of the rate performance of BZn||MnO_2 and GZn||MnO_2 full cells showed that the GZn||MnO_2 cell delivered superior capacities of 330.6, 311.9, 267.7, and 211.0 mA•h•g^{-1} under 0.5, 1, 2, and 5 A•g^{-1}, respectively, which was higher than those of the BZn||MnO_2 cell (Fig. S18). The voltage profiles of BZn||MnO_2 and GZn||MnO_2 cells showed 2 typical plateaus corresponding to the redox reactions observed in both charging and discharging curves at 0.5 A•g^{-1} (Fig. S19). With increasing current density, the polarization of the cell became more substantial, which was particularly clear for the BZn electrode. The CV curves of BZn||MnO_2 and GZn||MnO_2 cells exhibited a broad oxidation peak and 2 reduction peaks, corresponding to the charge and discharge plateaus in Fig. S9, respectively (Fig. S20). The CV curves were conducted after the cell rate performance test, and the shift of redox peak position reflected the degree of polarization of the full cell [5,36]. Herein, since the conditions for assembling the full cell were the same except for the anode, the anode was the main factor for the polarization difference of the cell. The uneven deposition on the surface of BZn anode reduced the charge transfer rate and Zn utilization rate, thus aggravating the polarization of the full cell [50–52]. The weaker polarization of the GZn electrode indicated that the generation of dendrites was prevented and the presence of Cu increased the conductivity of the electrode.

Discussion

In summary, a straightforward pressing method was used to prepare Cu-modified Zn anodes (GZn), and the effects of the added conductive grid Cu were investigated on the electrochemical performance of Zn anode. The results showed that close contact between the Cu mesh and Zn increased electrode conductivity and reduced the Zn plating/stripping overpotential of related symmetric cells. At the same time, Cu-mesh addition reduced hydrogen evolution and corrosion, thus delaying or avoiding the generation of by-products. After cycling, GZn presented a flat surface without dendrites. In addition, GZn||AC hybrid capacitors were assembled, which displayed a better cycling performance than BZn||AC hybrid capacitors due to the capable rate ability of GZn. Moreover, the potential application of GZn electrodes in Zn-ion batteries was also confirmed. This demonstrated that GZn appeared to be a promising universal anode for Zn-ion capacitors and batteries. In conclusion, this study provided a facile approach for achieving high-performance metal anodes.

Acknowledgments

Funding: This work was supported by the Hong Kong Scholars Programs (Grant No. XJ2019024), the Natural Science Foundation of Heilongjiang (LC2018004), Protective Materials Engineering Technology Research Center (002100130630D) and Heilongjiang Province Marine New Energy, the China Postdoctoral Science Foundation (2019T120254 and 2018M630340), and the Fundamental Research Funds for the Central University. **Author contributions:** Z.G.: Investigation and Writing original draft. Z.L.: Data curation. P.W.: Methodology and Funding acquisition. K.J. and Z.B.: Contributing analysis tools and Data analysis. K.Z.: Supervision, Methodology, and Review and editing. D.C.: Methodology and Review and editing. J.Y., K.Y., and G.W.: Formal analysis. G.C.: Supervision and Review and editing. **Competing interests:** The authors declare that they have no competing interests. **Data Availability:** All relevant data are within the manuscript and its additional files.

SUPPLEMENTARY MATERIALS

Figs. S1 to S20
Table S1

References

1. Wang H, Tan R, Yang Z, Feng Y, Duan X, Ma J. Stabilization perspective on metal anodes for aqueous batteries. *Adv Energy Mater*. 2020;11(2):Article 2000962.
2. Cao Z, Zhuang P, Zhang X, Ye M, Shen J, Ajayan PM. Strategies for dendrite-free anode in aqueous rechargeable zinc ion batteries. *Adv Energy Mater*. 2020;10(30):Article 2001599.
3. Gong Z, Jiang K, Wang P, Liu X, Wang D, Ye K, Zhu K, Yan J, Wang G, Cao D. Stable and dendrite-free Zn anode with artificial desolvation interface layer toward high-performance Zn-ion capacitor. *J Energy Chem*. 2022;72:143–148.
4. Hao J, Li B, Li X, Zeng X, Zhang S, Yang F, Liu S, Li D, Wu C. An in-depth study of Zn metal surface chemistry for advanced aqueous Zn-ion batteries. *Adv Mater*. 2020;32(34):Article 2003021.

5. Liang P, Yi J, Liu X, Wu K, Wang Z, Cui J, Liu Y, Wang Y, Xia Y, Zhang J. Highly reversible Zn anode enabled by controllable formation of nucleation sites for Zn-based batteries. *Adv Funct Mater*. 2020;30(13):Article 1908528.
6. Zhou Z, Zhang Y, Chen P, Wu Y, Yang H, Ding H, Zhang Y, Wang Z, du X, Liu N. Graphene oxide-modified zinc anode for rechargeable aqueous batteries. *Chem Eng Sci*. 2019;194:142–147.
7. Zhang Q, Luan J, Tang Y, Ji X, Wang H. Interfacial design of dendrite-free zinc anodes for aqueous zinc-ion batteries. *Angew Chem Int Ed*. 2020;59(32):13180–13191.
8. Zhao R, Yang Y, Liu G, Zhu R, Huang J, Chen Z, Gao Z, Chen X, Qie L. Redirected Zn electrodeposition by an anti-corrosion elastic constraint for highly reversible Zn anodes. *Adv Funct Mater*. 2020;31(2):Article 2001867.
9. Hieu L, So S, Kim I, Hur J. Zn anode with flexible β-PVDF coating for aqueous Zn-ion batteries with long cycle life. *Chem Eng J*. 2021;411:Article 128584.
10. Liu X, Yang F, Xu W, Zeng Y, He J, Lu X. Zeolitic imidazolate frameworks as Zn^{2+} modulation layers to enable dendrite-free Zn anodes. *Adv Sci*. 2020;7(21):Article 2002173.
11. Liu P, Zhang Z, Hao R, Huang Y, Liu W, Tan Y, Li P, Yan J, Liu K. Ultra-highly stable zinc metal anode via 3D-printed g-C_3N_4 modulating interface for long life energy storage systems. *Chem Eng J*. 2021;403:Article 126425.
12. Wang P, Gong Z, Ye K, Gao Y, Zhu K, Yan J, Wang G, Cao D. The stable lithium metal cell with two-electrode biomass carbon. *Electrochim Acta*. 2020;356:Article 136824.
13. Cao J, Zhang D, Zhang X, Sawangphruk M, Qin J, Liu R. A universal and facile approach to suppress dendrite formation for a Zn and Li metal anode. *J Mater Chem A*. 2020;8(18):9331–9344.
14. Wu B, Wu Y, Lu Z, Zhang J, Han N, Wang Y, Li XM, Lin M, Zeng L. A cation selective separator induced cathode protective layer and regulated zinc deposition for zinc ion batteries. *J Mater Chem A*. 2021;9(8):4734–4743.
15. Li Y, Tan Z, Liang Y, Xiao Y, Cen D, Liu Y, Liang Y. Amine-functionalized carbon cloth host for dendrite-free Zn metal anodes. *ACS Appl Energy Mater*. 2021;4(5):4482–4488.
16. Foroozan T, Yurkiv V, Sharifi-Asl S, Rojaee R, Mashayek F, Shahbazian-Yassar R. Non-dendritic Zn electrodeposition enabled by zincophilic graphene substrates. *ACS Appl Mater Interfaces*. 2019;11(47):44077–44089.
17. He H, Qin H, Wu J, Chen X, Huang R, Shen F, Wu Z, Chen G, Yin S, Liu J. Engineering interfacial layers to enable Zn metal anodes for aqueous zinc-ion batteries. *Energy Stor Mater*. 2021;43:317–336.
18. Shi X, Xu G, Liang S, Li C, Guo S, Xie X, Ma X, Zhou J. Homogeneous deposition of zinc on three-dimensional porous copper foam as a superior zinc metal anode. *ACS Sustain Chem Eng*. 2019;7(21):17737–17746.
19. Chen P, Yuan X, Xia Y, Zhang Y, Fu L, Liu L, Yu N, Huang Q, Wang B, Hu X, et al. An artificial polyacrylonitrile coating layer confining zinc dendrite growth for highly reversible aqueous zinc-based batteries. *Adv Sci*. 2021;8(11):Article e2100309.
20. Li Z, Wu L, Dong S, Xu T, Li S, An Y, Jiang J, Zhang X. Pencil drawing stable interface for reversible and durable aqueous zinc-ion batteries. *Adv Funct Mater*. 2020;31(4):Article 2006495.
21. Liu M, Yang L, Liu H, Amine A, Zhao Q, Song Y, Yang J, Wang K, Pan F. Artificial solid-electrolyte interface facilitating dendrite-free zinc metal anodes via nanowetting effect. *ACS Appl Mater Interfaces*. 2019;11(35):32046–32051.
22. Zhao Z, Zhao J, Hu Z, Li J, Li J, Zhang Y, Wang C, Cui G. Long-life and deeply rechargeable aqueous Zn anodes enabled by a multifunctional brightener-inspired interphase. *Energy Environ Sci*. 2019;12(6):1938–1949.
23. Yang Y, Liu C, Lv Z, Yang H, Zhang Y, Ye M, Chen L, Zhao J, Li CC. Synergistic manipulation of Zn^{2+} ion flux and desolvation effect enabled by anodic growth of a 3D ZnF_2 matrix for long-lifespan and dendrite-free Zn metal anodes. *Adv Mater*. 2021;33(11):Article e2007388.
24. Jian Q, Wan Y, Sun J, Wu M, Zhao T. A dendrite-free zinc anode for rechargeable aqueous batteries. *J Mater Chem A*. 2020;8(38):20175–20184.
25. Kim JY, Liu G, Shim GY, Kim H, Lee JK. Functionalized Zn@ZnO hexagonal pyramid array for dendrite-free and ultrastable zinc metal anodes. *Adv Funct Mater*. 2020;30(36):Article 2004210.
26. Li C, Shi X, Liang S, Ma X, Han M, Wu X, Zhou J. Spatially homogeneous copper foam as surface dendrite-free host for zinc metal anode. *Chem Eng J*. 2020;379:Article 122248.
27. Zhou Y, Wang X, Shen X, Shi Y, Zhu C, Zeng S, Xu H, Cao P, Wang Y, Di J, et al. 3D confined zinc plating/stripping with high discharge depth and excellent high-rate reversibility. *J Mater Chem A*. 2020;8(23):11719–11727.
28. Tian Y, An Y, Wei C, Xi B, Xiong S, Feng J, Qian Y. Flexible and free-standing $Ti_3C_2T_x$ MXene@Zn paper for dendrite-free aqueous zinc metal batteries and nonaqueous lithium metal batteries. *ACS Nano*. 2019;13(10):11676–11685.
29. Sun P, Ma L, Zhou W, Qiu M, Wang Z, Chao D, Mai W. Simultaneous regulation on solvation shell and electrode interface for dendrite-free Zn ion batteries achieved by a low-cost glucose additive. *Angew Chem Int Ed*. 2021;133(33):18395–18403.
30. Bayaguud A, Luo X, Fu Y, Zhu C. Cationic surfactant-type electrolyte additive enables three-dimensional dendrite-free zinc anode for stable zinc-ion batteries. *ACS Energy Lett*. 2020;5(9):3012–3020.
31. Han J, Mariani A, Varzi A, Passerini S. Green and low-cost acetate-based electrolytes for the highly reversible zinc anode. *J Power Sources*. 2021;485:Article 229329.
32. Huang J, Chi X, Du Y, Qiu Q, Liu Y. Ultrastable zinc anodes enabled by anti-dehydration ionic liquid polymer electrolyte for aqueous Zn batteries. *ACS Appl Mater Interfaces*. 2021;13(3):4008–4016.
33. Guo X, Zhang Z, Li J, Luo N, Chai GL, Miller TS, Lai F, Shearing P, Brett DJL, Han D, et al. Alleviation of dendrite formation on zinc anodes via electrolyte additives. *ACS Energy Lett*. 2021;6(2):395–403.
34. Wang J, Cai Z, Xiao R, Ou Y, Zhan R, Yuan Z, Sun Y. A chemically polished zinc metal electrode with a ridge-like structure for cycle-stable aqueous batteries. *ACS Appl Mater Interfaces*. 2020;12(20):23028–23034.
35. Wang A, Zhou W, Huang A, Chen M, Chen J, Tian Q, Xu J. Modifying the Zn anode with carbon black coating and nanofibrillated cellulose binder: A strategy to realize dendrite-free Zn-MnO_2 batteries. *J Colloid Interface Sci*. 2020;577:256–264.
36. Cao P, Zhou X, Wei A, Meng Q, Ye H, Liu W, Tang J, Yang J. Fast-charging and ultrahigh-capacity zinc metal anode for high-performance aqueous zinc-ion batteries. *Adv Funct Mater*. 2021;31(20):Article 2100398.
37. Cai Z, Ou Y, Wang J, Xiao R, Fu L, Yuan Z, Zhan R, Sun Y. Chemically resistant cu-Zn/Zn composite anode for long cycling aqueous batteries. *Energy Stor Mater*. 2020;27:205–211.

38. Yin Y, Wang S, Zhang Q, Song Y, Chang N, Pan Y, Zhang H, Li X. Dendrite-free zinc deposition induced by tin-modified multifunctional 3D host for stable zinc-based flow battery. *Adv Mater*. 2020;32(6):Article e1906803.
39. An Y, Tian Y, Li Y, Wei C, Tao Y, Liu Y, Xi B, Xiong S, Feng J, Qian Y. Heteroatom-doped 3D porous carbon architectures for highly stable aqueous zinc metal batteries and non-aqueous lithium metal batteries. *Chem Eng J*. 2020;400:Article 125843.
40. Zhang Q, Luan J, Fu L, Wu S, Tang Y, Ji X, Wang H. The three-dimensional dendrite-free zinc anode on a copper mesh with a zinc-oriented polyacrylamide electrolyte additive. *Angew Chem Int Ed*. 2019;58(44):15841–15847.
41. Xie F, Li H, Wang X, Zhi X, Chao D, Davey K, Qiao S-Z. Mechanism for zincophilic sites on zinc-metal anode hosts in aqueous batteries. *Adv Energy Mater*. 2021;11(9):Article 2003419.
42. Zhou S, Wang Y, Lu H, Zhang Y, Fu C, Usman I, Liu Z, Feng M, Fang G, Cao X, et al. Anti-corrosive and Zn-ion-regulating composite interlayer enabling long-life Zn metal anodes. *Adv Funct Mater*. 2021;31(46):Article 2104361.
43. Zeng X, Xie K, Liu S, Zhang S, Hao J, Liu J, Pang WK, Liu J, Rao P, Wang Q, et al. Bio-inspired design of an in situ multifunctional polymeric solid-electrolyte interphase for Zn metal anode cycling at 30 mA cm^{-2} and 30 mA h cm^{-2}. *Energy Environ Sci*. 2021;14:5947–5957.
44. Huang F, Li X, Zhang Y, Jie Y, Mu X, Yang C, Li W, Chen Y, Liu Y, Wang S, et al. Surface transformation enables a dendrite-free zinc-metal anode in nonaqueous electrolyte. *Adv Mater*. 2022;34(34):Article 2203710.
45. Li Z, Gong Z, Wu X, Ye K, Yan J, Wang G, Wei Y, Zhu K, Yi J, Cao D, et al. Dendrite-free and anti-corrosion Zn metal anode enabled by an artificial layer for high-performance Zn ion capacitor. *Chin Chem Lett*. 2022;33(8):3936–3940.
46. Sun K, Hoang T, Doan T, Yu Y, Zhu X, Tian Y, Chen P. Suppression of dendrite formation and corrosion on zinc anode of secondary aqueous batteries. *ACS Appl Mater Interfaces*. 2017;9(11):9681–9687.
47. Han D, Wu S, Zhang S, Deng Y, Cui C, Zhang L, Long Y, Li H, Tao Y, Weng Z, et al. A corrosion-resistant and dendrite-free zinc metal anode in aqueous systems. *Small*. 2020;16(29):Article 2001736.
48. Xie X, Liang S, Gao J, Guo S, Guo J, Wang C, Xu G, Wu X, Chen G, Zhou J. Manipulating the ion-transfer kinetics and interface stability for high-performance zinc metal anodes. *Energy Environ Sci*. 2020;13(2):503–510.
49. Li C, Xie X, Liang S, Zhou J. Issues and future perspective on zinc metal anode for rechargeable aqueous zinc-ion batteries. *Energy Environ Mater*. 2020;3(2):146–159.
50. Wang P, Liang S, Chen C, Xie X, Chen J, Liu Z, Tang Y, Lu B, Zhou J. Spontaneous construction of nucleophilic carbonyl-containing interphase toward ultrastable zinc-metal anodes. *Adv Mater*. 2022;34(33):Article 2202733.
51. Liang G, Zhu J, Yan B, Li Q, Chen A, Chen Z, Wang X, Xiong B, Fan J, Xu J, et al. Gradient fluorinated alloy to enable highly reversible Zn-metal anode chemistry. *Energy Environ Sci*. 2022;15:1086–1096.
52. Xiao P, Li H, Fu J, Zeng C, Zhao Y, Zhai T, Li H. An anticorrosive zinc metal anode with ultra-long cycle life over one year. *Energy Environ Sci*. 2022;15:1638–1646.